



## PAPER

## Investigation of optical fiber-tip probes for common and ultrafast SERS

## OPEN ACCESS

## RECEIVED

28 November 2019

## REVISED

9 February 2020

## ACCEPTED FOR PUBLICATION

2 March 2020

## PUBLISHED

23 March 2020

Original content from this work may be used under the terms of the [Creative Commons Attribution 4.0 licence](https://creativecommons.org/licenses/by/4.0/).

Any further distribution of this work must maintain attribution to the author(s) and the title of the work, journal citation and DOI.

Yevhenii M Morozov<sup>1,2,4</sup> , Anatoliy S Lapchuk<sup>2</sup>, Alexander V Prygun<sup>2</sup>, Andriy A Kryuchyn<sup>2</sup> and Jakub Dostalek<sup>3</sup><sup>1</sup> College of Science, Zhejiang University of Technology, 288 Liuhe Road, 310023 Hangzhou, People's Republic of China<sup>2</sup> Institute for Information Recording of NAS of Ukraine, 2 Shpaka Street, 03113 Kiev, Ukraine<sup>3</sup> Biosensor Technologies, AIT-Austrian Institute of Technology GmbH, 24 Konrad-Lorenz-Strasse, A-3430 Tulln, Austria<sup>4</sup> Current address: 'Institute for Information Recording of NAS of Ukraine, 2 Shpaka Street, 03113 Kiev, Ukraine' only.E-mail: [morozov.ye.m@gmail.com](mailto:morozov.ye.m@gmail.com)**Keywords:** femtosecond pulse, gold nanoparticles, optical fiber-tip probe, surface-enhanced Raman spectroscopy, temporal response, ultrafast nanophotonics**Abstract**

In this study, we performed a three-dimensional computational experiment on ultrashort pulse propagation in an optical fiber-tip probe that is decorated with gold nanoparticles (NPs) using a constant structure for the probe's dielectric taper and different spatial configurations of the gold nanoparticles. Interestingly, a hot spot with the highest amplitude of the electric field was found not along the same chain of the NPs but between terminal NPs of neighboring chains of NPs at the probe's tip (the amplitude of the electric field in the hot spots between the NPs along the same chain was of the order of  $10^1$ , while that between terminal NPs of neighboring chains was of the order of  $10^3$ ). We eventually identified a configuration with only six terminal nanoparticles (Config4) which is characterized by the highest electric field amplitude enhancement and can provide the highest spatial resolution in the SERS interrogation of an object of interest. The ultrashort temporal responses of the hot spots for all configurations exhibited relatively high pulse elongation (relative elongation was greater than 4.3%). At the same time, due to the reflection of the incident pulse and consequent interference, the temporal responses of most hot spots contained several peaks for all configurations except for the optimum Config4. Nonetheless, the ultrashort temporal responses of all hot spots for Config4 were characterized by a single peak but with a relatively large pulse elongation (relative elongation was 234.1%). The results indicate that further examination of this new structure of a nanoparticles-coated optical fiber-tip probe with only six terminal NPs may provide attractive characteristics for its practical applications.

**1. Introduction**

Raman spectroscopy is a powerful technique for revealing intrinsic local chemical information in different types of systems, and is important in physics, material science, chemistry, biology, and medicine [1–11]. As spontaneous Raman signal is inherently weak, different types of Raman spectroscopy have been proposed and developed, such as surface-enhanced [12–15], tip-enhanced [16, 17], femtosecond-stimulated [18–20], femtosecond time-resolved impulsive stimulated [21], polarized [22, 23], and shifted excitation [24, 25] Raman spectroscopy. Recently, in surface-enhanced Raman spectroscopy (SERS), the so-called 'nanopipette' structures [26, 27] and nanoparticles-coated optical fiber-tip probes have garnered significant interest [28–31]. Hutter *et al* [32] provided a systematic study of gold nanoparticles-coated optical fiber-tip probes by means of a two-dimensional (2D) numerical simulation. However, 2D analysis gives only qualitative insight into a process or device and cannot provide a full description. Moreover, the ultrashort pulse delivery capability of such Raman probes remains unclear. In [32], the model used for analysis contained an 'ideal' arrangement of NPs that is impossible to achieve in experiment. From this ideal arrangement, it is unclear whether the NPs behave like a

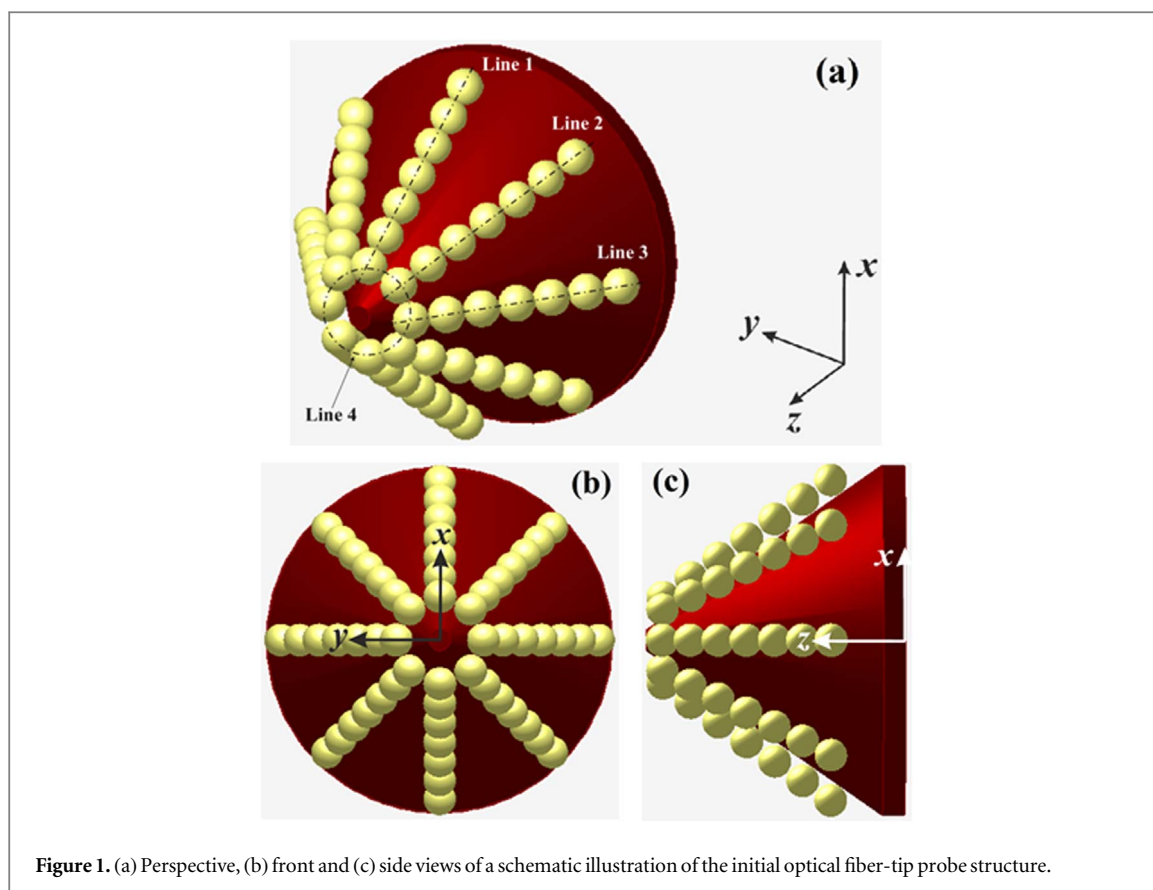


**Figure 1.** (a) Perspective, (b) front and (c) side views of a schematic illustration of the initial optical fiber-tip probe structure.

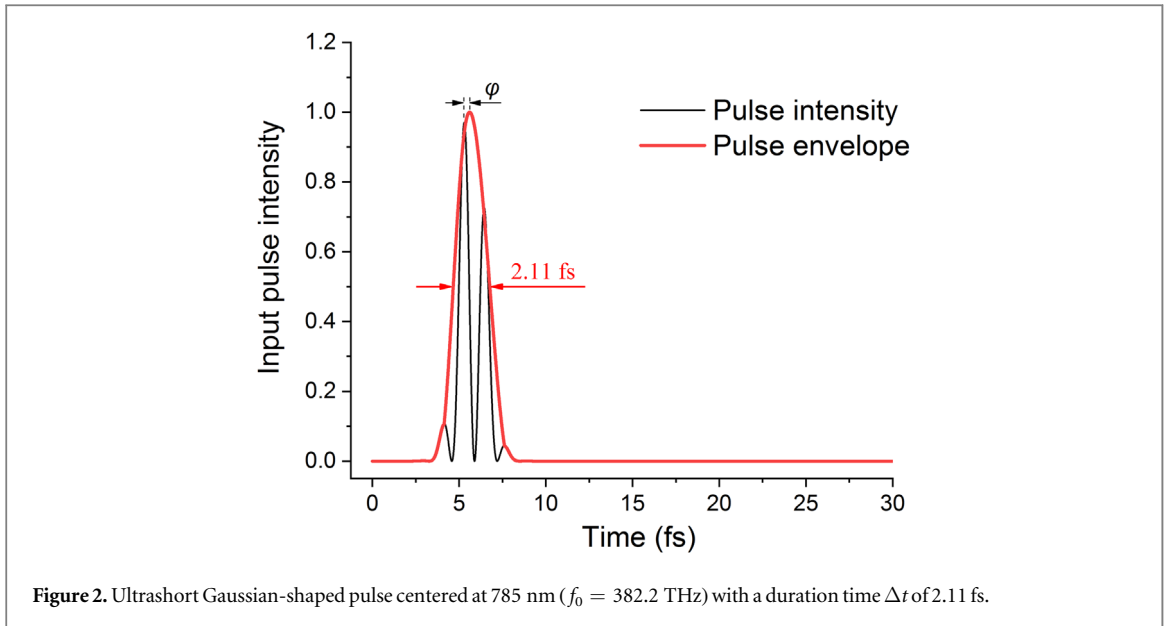
coupled chain or like separate NPs. In this study, we report a novel 3D computational experiment on ultrashort pulse (2.11 fs at the FWHM intensity level) propagation through an optical fiber-tip probe decorated with gold nanoparticles using a constant structure of the probe's dielectric taper but different configurations of the arrangement of NPs, and reveal parameters such as electric field enhancement and temporal ultrashort pulse characteristics. Moreover, we eventually identified a new structure consisting of only six terminal NPs and demonstrate its potential in practical applications.

## 2. Details of numerical simulation

The analysis was based on the numerical solution of Maxwell's linear equations by the 3D finite-difference time-domain method [33]. The Drude–Lorentz model [34] was used to describe the interaction of the metal with electromagnetic radiation. The parameters of the fused silica used were taken from [35] and those of gold from [36]. The choice of the Drude–Lorentz model and parameters of gold from work by Johnson and Christy were dictated by the desire to fit the complex dielectric function of gold correctly [37], as this is crucial for the considered structure (especially at the femtosecond scale [38]). To fit the dielectric function of the fused silica, we used the multi-coefficient model [39].

In figure 1, the initial ('ideal') optical fiber-tip probe model used for simulation is presented. The NPs were arranged to form eight lines (chains). However, due to the symmetry of the structure with respect to planes  $x = 0$  and  $y = 0$ , and the axis of rotation, we are interested only in three chains of gold nanoparticles intersected in figure 1 by Lines 1, 2, and 3. This initial configuration is extremely convenient to perform such an analysis as it allows—by gradually removing certain nanoparticles—to track the position and behavior of the hot spots and establish their ultrafast characteristics. At the same time, from the experimental point of view, this initial NP arrangement can be considered as an averaged arrangement of NPs on the optical fiber-tip probe surface, while all other configurations (see next section) can be attributed to inaccuracies in the manufacturing of such structures.

To reduce the calculation time, the electric and magnetic walls were placed in the planes of symmetry,  $y = 0$  and  $x = 0$ , respectively. Note that these conditions corresponded to the case of laser excitation with polarization along the  $x$ -axis. All boundaries of the simulation cube contained perfectly matched layers and were set more than 400 nm from the surfaces of the metal structure to avoid the absorption of near fields. The convergence of the numerical results and the mesh adaptation of the models used were analyzed before the simulation (note that



the smallest mesh step of 0.073 nm was set in between NPs to ensure the accuracy of the simulation). The meaning of Line 4 (see figure 1) will become clear from further discussion (it is worth noting that although the name ‘Line 4’ is not geometrically correct, we preferred to use this name in order to preserve the unity of the names of the considered curves).

The optical fiber-tip probe consisted of a conical tapered fused silica fiber tip that is decorated with several chains of gold nanoparticles. Each chain consisted of seven NPs. The numbering of the NPs started from the probe’s tip, i.e. the third nanoparticle from the tip across Line 1 was labeled NP-1\_3, the second nanoparticle from the tip across Line 2 as NP-2\_2, and so on. The diameter of the spherical NPs ( $2a$ ,  $a$  is the radius) was 150 nm, tip convergence semi-angle was  $35^\circ$ , and a gap of 5 nm between NPs in individual chains was chosen as Hutter *et al* claimed that this is the optimal configuration and these NPs are resonant at 785 nm [32]. The gold NPs were placed 1 nm from the conical fiber surface. However, note that owing to a lack of space, the diameter of the starting (closest to the probe’s tip) nanoparticles NP-2\_1, NP-4\_1, NP-6\_1, and NP-8\_1 was reduced to 148 nm to avoid intersection between NP-1\_1 and NP-3\_1, NP-3\_1 and NP-5\_1, NP-5\_1 and NP-7\_1, and NP-7\_1 and NP-1\_1, respectively. It also led to the distance between the NPs at the probe’s tip being as small as 0.82 nm (as this value is very close to 1 nm, non-local dielectric effects can be neglected [40]). The material surrounding the NPs was air. The initial and terminal diameters of the conical fiber tip were set to 1600 and 100 nm, respectively.

The electric field of the electromagnetic wave of a pulse produced by an ultrafast laser can be expressed in the following form [41]:

$$E^{\text{input}}(t) = A(t)\sin(\omega_0 t + \varphi), \quad (1)$$

where  $A(t)$  is the shape envelope of the pulse,  $\omega_0$  is the carrier frequency at the center of the laser’s emission spectrum, and  $\varphi$  is the phase offset between the envelope’s maximum and the nearest maximum of the carrier frequency. The appearance of a phase offset is related to the fact that the envelope travels at the group velocity while the carrier frequency moves at the phase velocity. Because of dispersion in the resonator, these velocities are different. In our simulation, to excite the structures under consideration, we used an ultrashort Gaussian-shaped pulse centered at a wavelength in vacuum of 785 nm ( $f_0 = 382.2$  THz) with an FWHM duration time  $\Delta t$  of 2.11 fs (see figure 2). Such ultrashort pulse was considered due to the fact that optical pulses of such duration possess high potential in ultrafast nanophotonics [42], as ultrafast science is rapidly moving toward increasingly complex systems [43], such as multiphoton microscopy in membranes and cells, quantum networks in diamond, or excitonic coherence in photosynthesis. Despite the fact that in some cases [44] pulses with duration of  $>1$  fs undergo barely noticeable degradation during propagation to the optical fiber extremities, pulse elongation in a fiber is strongly dependent on the fiber structure. Therefore, in our case pulse at the fiber tip can be broadened (as it has no cladding layer with relatively large convergence semi-angle of  $35^\circ$ ) and this effect will be considered in the next section. Note that unless specified, all amplitudes and intensities in the study were normalized to the maximum values of the input pulse.

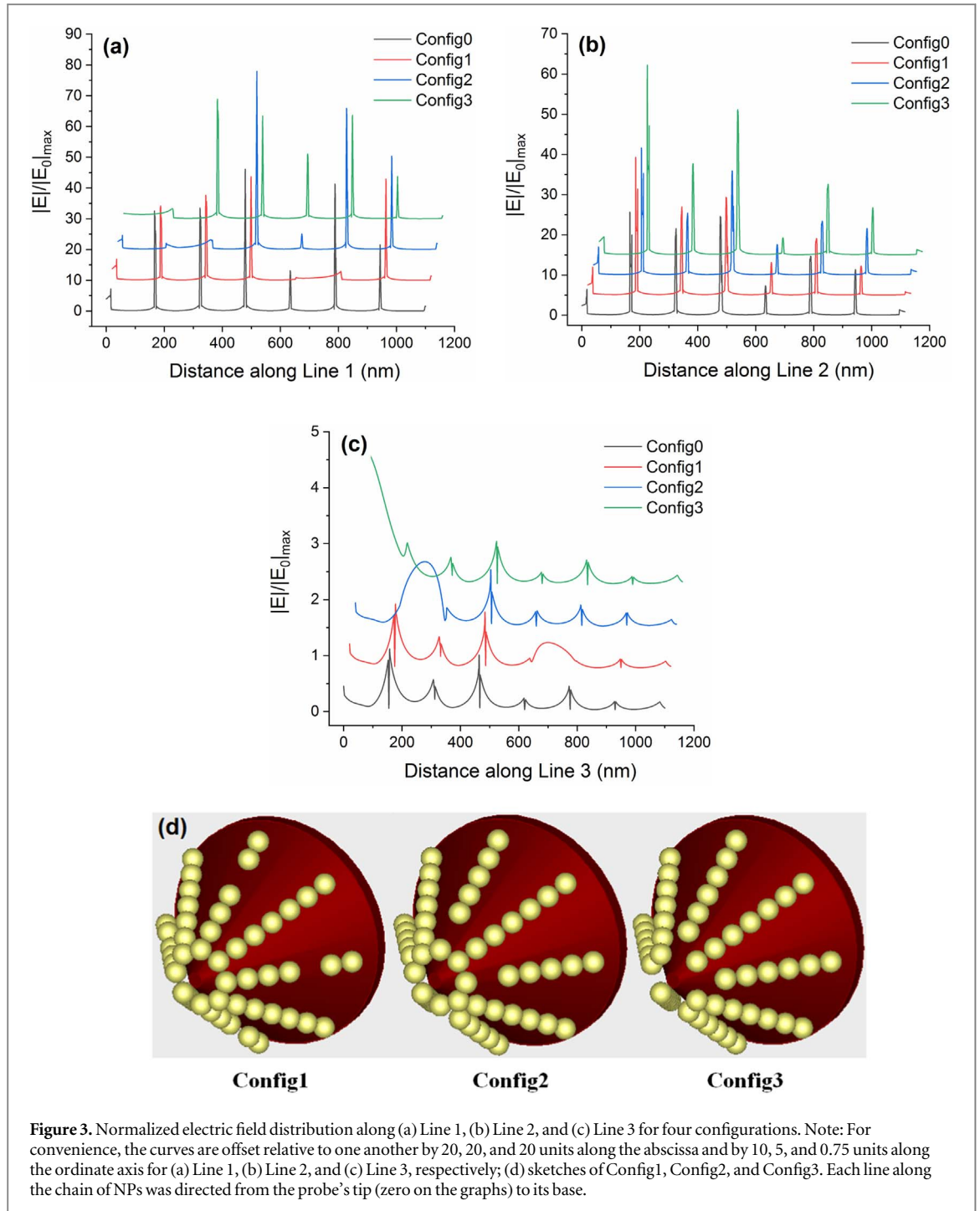


**Figure 3.** Normalized electric field distribution along (a) Line 1, (b) Line 2, and (c) Line 3 for four configurations. Note: For convenience, the curves are offset relative to one another by 20, 20, and 20 units along the abscissa and by 10, 5, and 0.75 units along the ordinate axis for (a) Line 1, (b) Line 2, and (c) Line 3, respectively; (d) sketches of Config1, Config2, and Config3. Each line along the chain of NPs was directed from the probe's tip (zero on the graphs) to its base.

### 3. Results and discussion

#### 3.1. Analysis of hot spot distribution in 3D optical fiber-tip probes

Figure 3 shows the normalized electric field distribution along (a) Line 1, (b) Line 2, and (c) Line 3 for four configurations: initial (Config0); Config1, which was Config0 without NP-1\_5, NP-3\_5, NP-5\_5, and NP-7\_5; Config2, which was Config0 without NP-1\_2, NP-3\_2, NP-5\_2, and NP-7\_2; and Config3, which was Config0 without NP-1\_1, NP-3\_1, NP-5\_1, and NP-7\_1 (see sketches in figure 3(d)). Note that the fifth, second, and first NPs were removed from Lines 5 and 7 for Config1, Config2, and Config3, respectively, to preserve the symmetry of the structure. Note that the distributions of the instantaneous values of the electric field are shown for the central wavelength ( $\lambda_0 = 785$  nm); therefore, they might not have been the maximum values over the entire frequency range of the input pulse. Each line along the chain of NPs was directed from the probe's tip to its base.

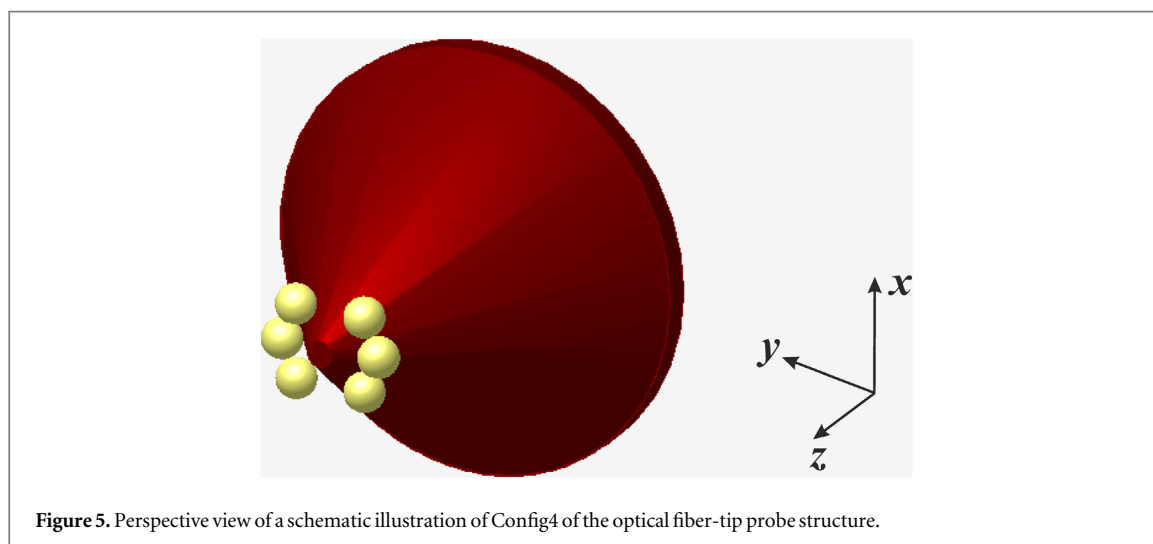
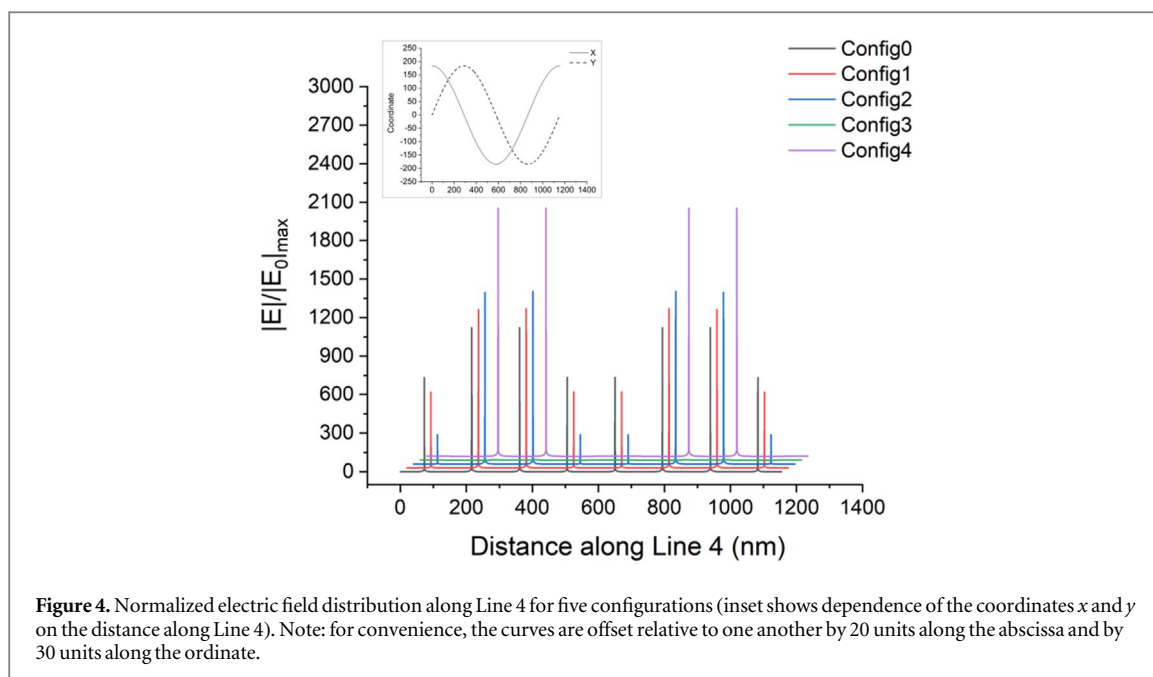
To interpret the results shown in figure 3, it is useful to consider the analyzed structure as follows: The structure of the origin (Config0) can be represented as a system of the tapered (conic) dielectric waveguide and

seven-nanoparticle chain waveguides [45] coupled to the conic waveguide. The spherical metallic nanoparticle chain can have longitudinal and transverse modes. In the case of a chain with a small distance  $d$  between adjacent particles (gap between adjacent particles is significantly smaller than particle diameter  $2a$ :  $d \ll 2a$ ; 5 nm  $\ll$  150 nm), the field of the longitudinal mode of the spherical nanoparticle chain is concentrated in the gap and creates a hot spot. In this way, a propagating plasmon wave is excited at each NP in a chain as a result of the interactions of particle chains with light beam in the conic dielectric waveguide. The cross-section of the dielectric waveguide is significantly larger than that of the NP chain waveguides (excluding the probe's apex). Therefore, the NP chain waveguides have a small influence on light propagation in the tapered dielectric waveguide. Light propagating in the conic waveguide is concentrated at the cone's apex. The longitudinal modes of the chain waveguides are excited at each NP in the chain and travel along the chain in the form of propagating plasmon waves with attenuation. However, owing to the increasing field intensity in the conic waveguide as it narrows, the amplitude of the excited field at each new NP increases, and coherently interferes with the field already guided inside the NP chain waveguide. The longitudinal mode reflects from the chain end creating a standing wave at the probe's apex with a field intensity antinode (maximum) (between the first and second particles in our nomenclature) [45]. According to this simplified model, we obtained similar field distributions along Line 2 (figure 3(b)) for all considered configurations. At the same time, we expected a larger difference in field amplitudes along Line 1 for different configurations due to the gap inside the chain waveguide if a nanoparticle was removed. This large gap leads to an increased  $b$  to  $a$  ratio [42], where  $b$  is the center-to-center (of NPs) distance and  $a$  is the radius of the NP. In other words, this large gap acts as the termination of the NP chain waveguide and lead to the propagating plasmon wave reflecting from it, which increased the amplitude of the previous hot spot. However, the overall difference was not drastically different because the main contribution to hot spot intensities caused the electric field in the conical waveguide near the probe's apex to increase. All predictions of this simplified theory are shown in figures 3(a) and (b) and are as follows: (1) The normalized electric field distribution along Line 2 (see figure 3(b)) is more or less the same for all considered configurations. (2) In a normalized electric field distribution along Line 1 (see figure 3(a)), there is a slight increase in amplitude for the hot spot located just before the removed nanoparticle. (3) Qualitatively, the amplitude distribution along Line 1 is identical for all configurations. Note that because of the same condition ( $d \ll 2a$ ), the interference effects of scattered fields will not occur [46] for the considered structure, leading to easier far-field detection of signals in a SERS setup.

For the normalized electric field amplitude distribution along Line 3 (see figure 3(c)), electric field enhancement was low ( $\leq 1$ ). This can be explained by two observations: (1) The main component of the electric field of the longitudinal mode in the gap is in the direction parallel to the chain axis, which is orthogonal to the electric intensity vector of the linear polarized wave guided by the dielectric conical fiber tip. Therefore, the main component of the electric field of the longitudinal mode was zero in this line and only a weak excitation of the transverse modes occurs leading to insignificant field enhancement. The transverse nature of the modes is apparent from the fact that the field intensity drops to zero in the center of gap between NPs, see figure 3(c). The removal of an NP did not lead to any change in the field distribution as these modes were not coupled together and did not contribute to forming a propagating plasmon wave. Moreover, the electric field was stronger along the edge of the NPs but nearly equal to zero in between them. This conclusion is supported by Liu *et al* [31], where higher SERS signals were obtained for the azimuthal vector mode  $TE_{01}$  that for the linear  $HE_{11}$  mode as a result of the larger effective SERS area in this case. Therefore, owing to the low electric field amplitude of these hot spots, we will not consider them further.

Importantly, we observed that the most intense coupled LSP field was observed not in between NPs along the same chain (Lines 1–3), but in between neighboring NPs of different chains at the probe's tip (along Line 4, see figure 4). Line 4 had the form of a circle and connected the centers of eight terminal NPs of the initial configuration (thus, it lies in a plane that divides the nanoparticles in half) (see figure 1(a)). Line 4 had a radius of 183.52 nm. This phenomenon can be explained by two factors: (1) The first one is the smaller distance between NPs along Line 4 (0.82 nm) in comparison with the 5 nm along Lines 1–3. (2) The second one: Due to the above-mentioned polarization projection issue, the projection of the  $x$ -component of the electric field on the direction of the straight line connecting the centers of the corresponding NPs was the maximum of all cases. Figure 4 shows the normalized electric field amplitude distribution along Line 4 for five configurations: four of them (Config0–Config3) are the same as before, and Config4 is a configuration with only six terminal NPs (see figure 5). The starting point of Line 4 in figure 4 was defined as the center of nanoparticle NP-1\_1 with anti-clockwise bypass (dependence of the coordinates  $x$  and  $y$  on the distance along Line 4 is shown in the figure's inset).

From figure 4, it is clear that the distribution of electric field amplitude enhancement is almost identical for Config0–Config2. For Config3, there is no hot spot due to the absence of the corresponding NPs. Config4 is characterized by the presence of four hot spots only between the corresponding nanoparticles (between NP-2\_1 and NP-3\_1, NP-3\_1 and NP-4\_1, NP-6\_1 and NP-7\_1, and NP-7\_1 and NP-8\_1) and higher normalized



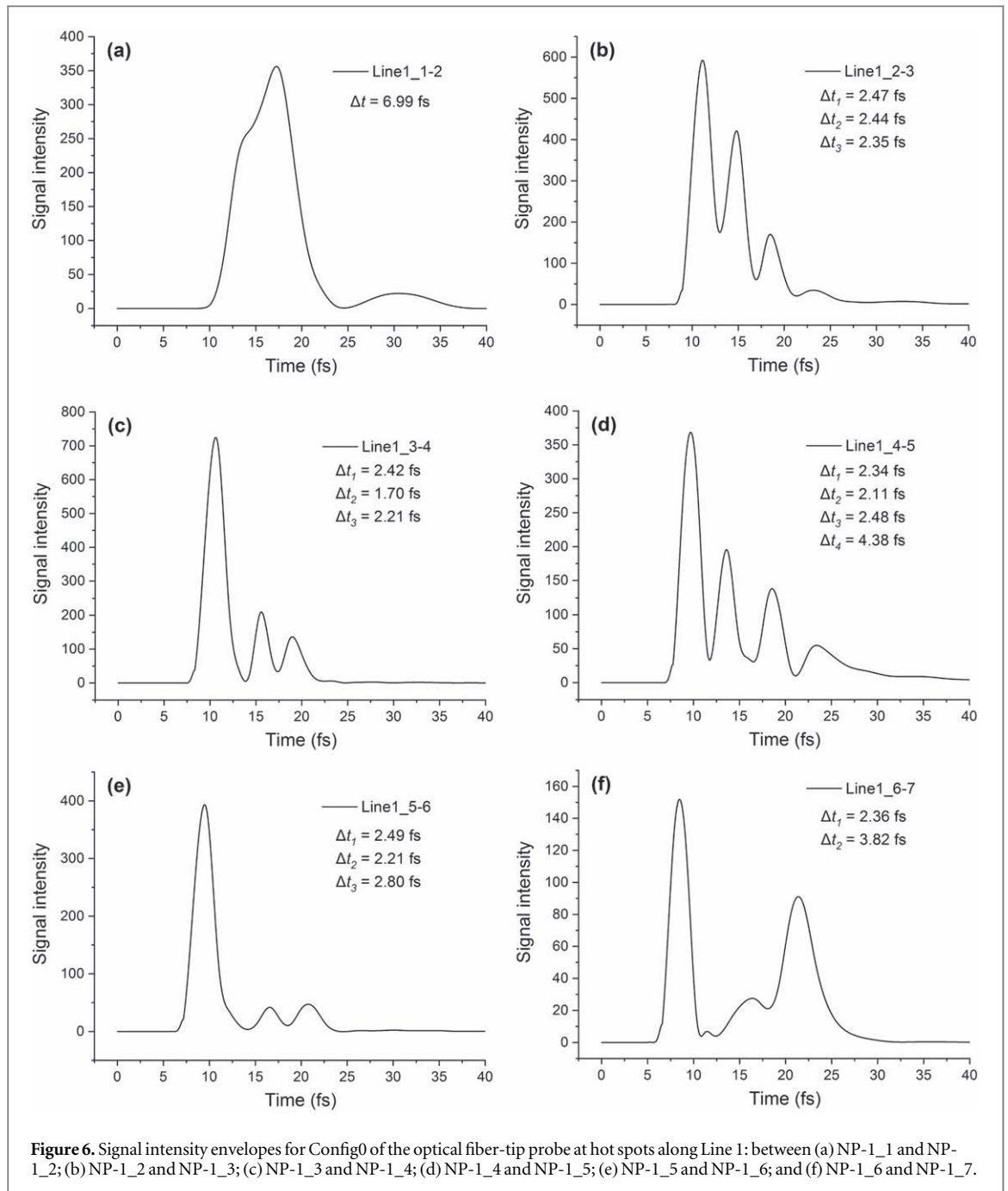
amplitudes than other configurations (increasing from 1121.73 for Config0 to 1934.54 for Config4). Such an increase in the electric field amplitude enhancement for Config4 can be explained by the fact that more energy of the fundamental  $HE_{11}$  mode reaches the tip of the probe, which lead to a more intense excitation of the corresponding coupled LSPs. For Config4, the electric field enhancement is as high as 2000; that is, the intensity at these points increases by  $\approx 4.0 \times 10^6$  times. It is also worth noting that Config4 could potentially provide a higher spatial resolution than the other configurations because it has more localized hot spots, while effective SERS area will be smaller. However, this smaller effective SERS area can be balanced by a more intense SERS signal in this case. Therefore, this increased spatial resolution can be useful for practical applications because the SERS signal is highly sensitive to the location of the SERS fiber-tip probe in a living cell [27].

### 3.2. Ultrafast temporal responses of hot spots in 3D optical fiber-tip probes

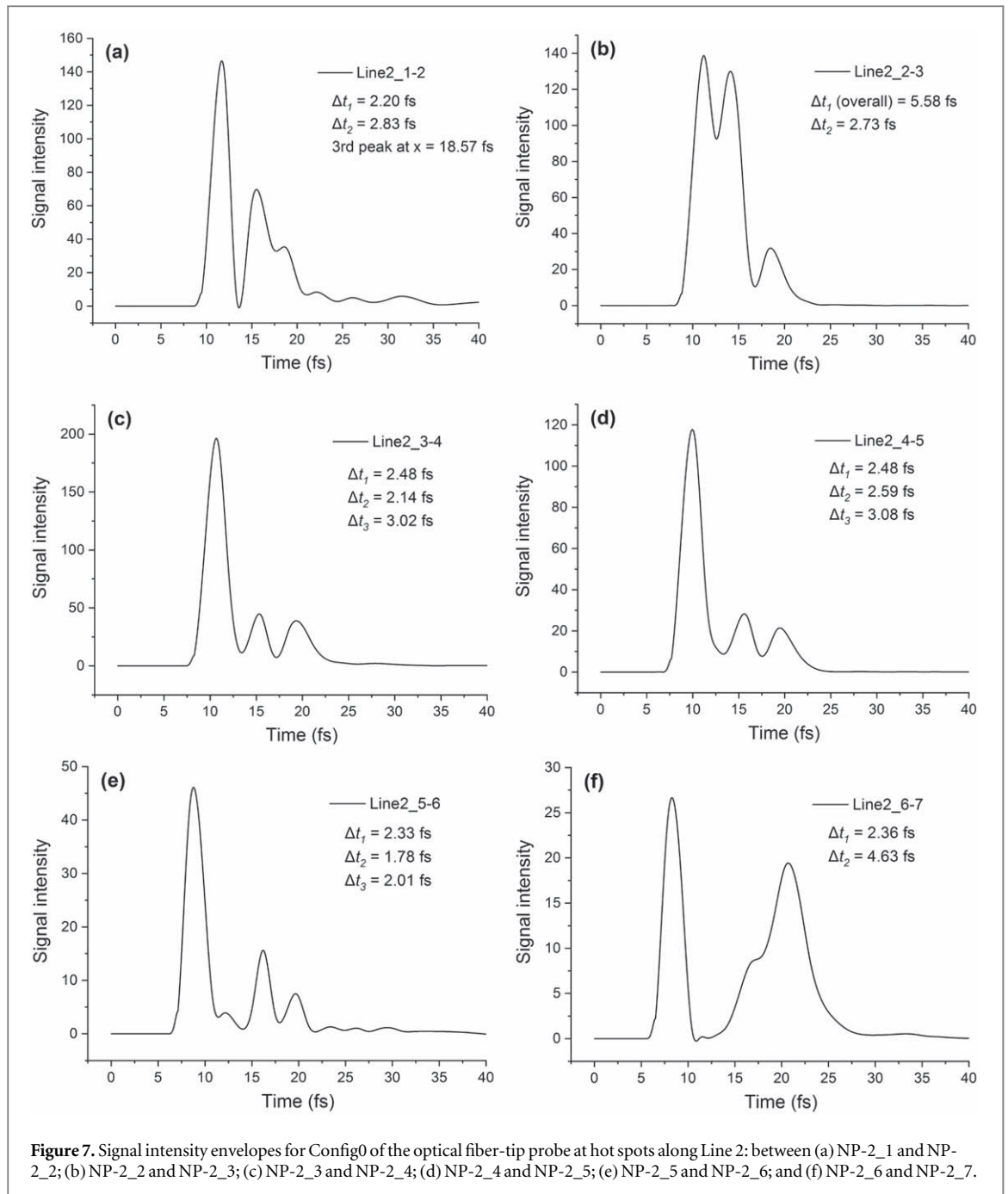
We also considered ultrafast temporal responses of hot spots analyzed in the previous subsection. Figure 6 shows the signal intensity envelopes for Config0 of the optical fiber-tip probe at hot spots along Line 1. The nomenclature used here is as follows: Line1\_1–2 represents the hot spot between NP-1\_1 and NP-1\_2, Line1\_2–3 represents the hot spot between NP-1\_2 and NP-1\_3, and so on.

Figure 7 shows the signal intensity envelopes for Config0 of the optical fiber-tip probe at hot spots along Line 2.

From figures 6 and 7 it is clear that most of the hot spots along Lines 1 and 2 are characterized by more than single-peak responses and relatively pronounced elongation. However, some of these configurations exhibit a



near-single-peak shape (see figure 6(a): the absolute and relative elongations are 4.88 fs and 231.3%, respectively) and relatively minimized elongation (see figure 7(a): absolute and relative elongations are only 0.09 fs and 4.3%, respectively). Signals along Line 1 (figure 6) can be explained as follows: When reaching the apex of the probe, the input pulse has almost the same form as at the start of the probe with an increased duration (see figure 6(a)). The pulse is partially reflected from the probe's apex, and has an electric field amplitude in the form of  $E_0(1 + R)$ , where  $E_0$  is the electric field amplitude of the incident pulse and  $R$  is the complex reflection coefficient with a small phase because there is a node of field of the longitudinal mode at the end of the chain [45]. In this way, due to reflection, the amplitude of the reflected pulse is slightly amplified. Further, between NP-1\_1 and NP-1\_2 (see figure 6(b)), a phase shift occurs between the fields of the incident and reflected pulses because of the distance to the end of the chain, and peaks of the incident and reflected pulses passes through this measurement point at different times. Due to interference between the incident and reflected pulses and time differences, the signals differ from one measurement point to another (from one gap in between NPs to another). In this way, all signals except the last one (figure 6(a)) result from this interference. The signal in the gap between NP-1\_6 and NP-1\_7 (see figure 6(f)) consists of two pulses: the first one is the incident pulse and the



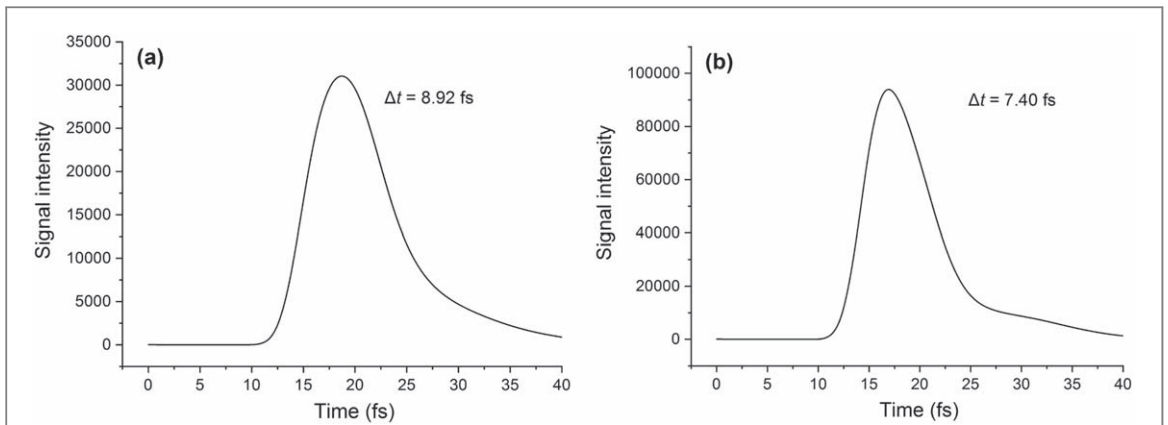
second the back-reflected pulse. Note that the back-reflected pulse is also amplified in this case as the area near that gap is practically another terminal of the NP chain, and is where the second reflection occurs.

Figure 8 shows signal intensity envelopes for Config4 of the optical fiber-tip probe at hot spots between (a) NP-1\_1 and NP-2\_1 (this position corresponds to the first peak in figure 4), and (b) NP-2\_1 and NP-3\_1 (this position corresponds to the second peak in figure 4).

From figures 8(a), (b) it is clear that temporal responses for these hot spots have single-peaked shapes. However, the absolute elongations are 6.81 and 5.29 fs, and the relative elongations are 322.7% and 250.7% for (a) and (b), respectively.

In order to understand the reasons for noticeable pulse elongation for all configurations more deeply, we performed an analysis of the pulse propagation in the fiber-tip probe alone (without nanoparticles at its surface). Figure 9 illustrates the signal intensity envelopes for the bare fiber-tip probe at the base (black curve) and at the tip (red curve) of the fiber.

From figure 9, the absolute elongation is 0.69 fs and the relative elongation is 32.7% for output pulse (with the relatively low electric field enhancement of 2.21). This pulse elongation in the fiber alone may be the main reason for the pulse elongation for different configurations. In addition, group velocity of wave in the fiber



**Figure 8.** Signal intensity envelopes of the optical fiber-tip probe for Config4 at hot spots between (a) NP-1\_1 and NP-2\_1 (corresponding to the first peak in figure 4), and (b) NP-2\_1 and NP-3\_1 (corresponding to the second peak in figure 4).

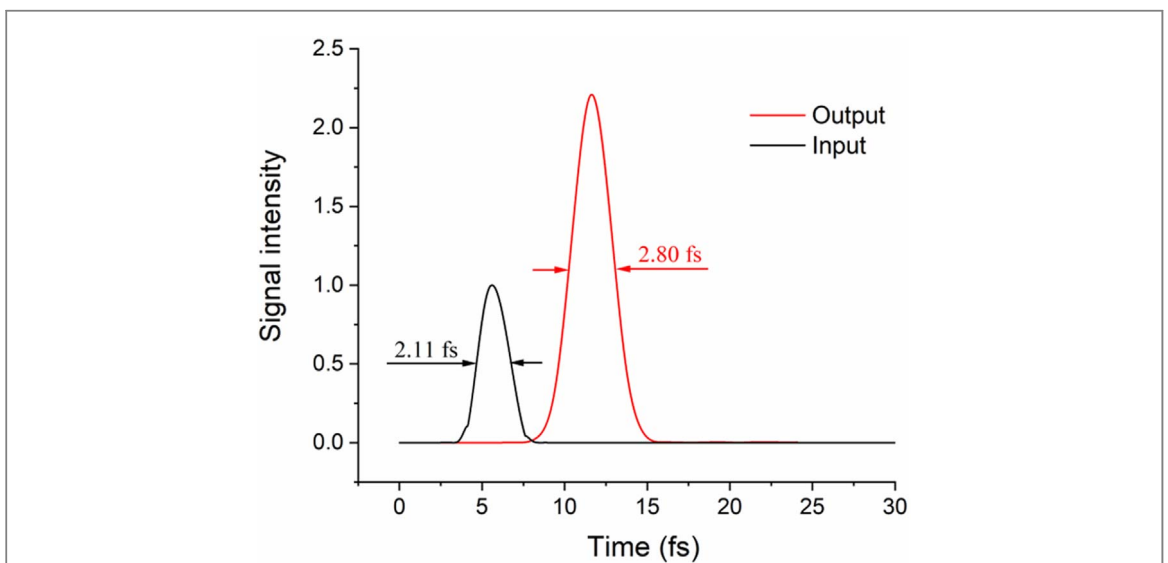


**Figure 9.** Signal intensity envelopes for the bare fiber-tip probe (without nanoparticles at its surface) at the base (black curve) and at the tip (red curve) of the fiber.

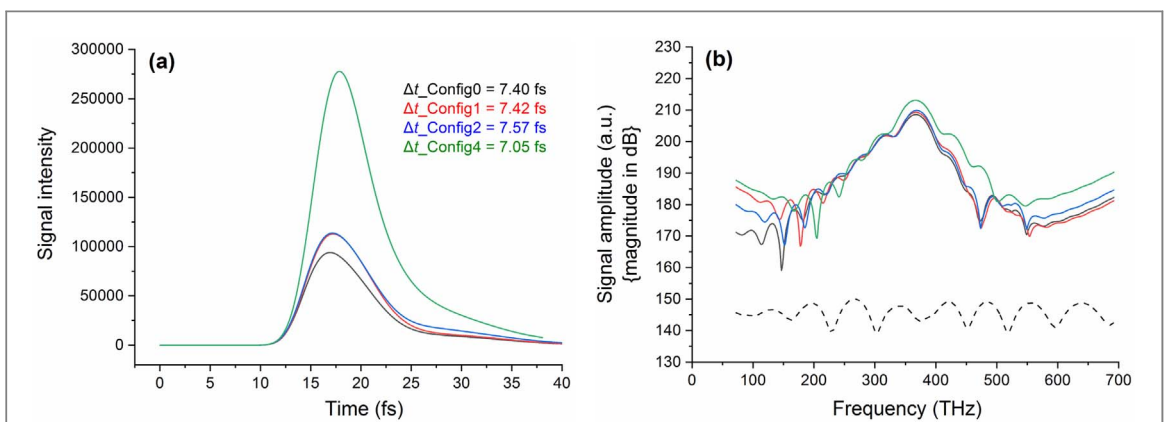


**Figure 10.** (a) Signal intensity envelopes and (b) spectral dependence of amplitude at the hot spot between NP-2\_1 and NP-3\_1 at the highest intensity (corresponding to the second peak in figure 4) for four configurations: Config0 (black curve), Config1 (red curve), Config2 (blue curve), and Config4 (green curve). The broken black curve in (b) corresponds to the spectral dependence of the amplitude of the input signal. Note: amplitudes in (b) were not normalized to the maximum input value.

differs from phase velocities of longitudinal and transverse modes in the NP chains. It leads to additional optical path differences in mode propagation (besides note the mode re-reflection in each gap between nanoparticles) and to the pulse broadening. However, more rigorous and detailed analysis is required in the future to understand the pulse propagation process in such a structure in more detail.

Figure 10 shows (a) the signal intensity envelopes and (b) the spectral dependence of amplitude at the hot spot between NP-2\_1 and NP-3\_1 at the highest intensity (this position corresponds to the second peak in figure 4) for four configurations: Config0 (black curve), Config1 (red curve), Config2 (blue curve), and Config4 (green curve). The broken black curve in figure 10(b) corresponds to the spectral dependence of the amplitude of the input signal.

From figure 10, it is clear that the signal is qualitatively identical for all considered configurations, which coincides with the results of section 3.1. A drop above 400 THz can be attributed to the increased loss in gold nanoparticles starting at these frequencies. Note that knowledge of  $E^{\text{input}}(\omega)$  and  $E^{\text{output}}(\omega)$  gives the ability to calculate the so-called impulse response function [47] and, therefore, to perform the requisite laser pulse shaping to obtain an output pulse with the desired shape.

## 4. Conclusion

In this study, we performed a 3D computational experiment on ultrashort pulse propagation through gold nanoparticles (NPs)-coated optical fiber-tip probes with a constant structure of the probe's dielectric taper but different configurations of the arrangement of the NPs. A hot spot with the highest amplitude of the electric field was found not along the same chain of the NPs but between terminal NPs of neighboring chains at the probe's tip (the amplitude of the electric field in the hot spots between the NPs along the same chain was of the order of  $10^1$ , while that between terminal NPs of neighboring chains was of the order of  $10^3$ ). Consequently, we identified a configuration with only six terminal nanoparticles (Config4 in the main text) which shows the advantage of the highest enhancement in the electric field amplitude and holds potential to provide the highest spatial resolution during the SERS analysis of the object of interest (such as a live cell).

As for the ultrashort optical pulse characteristics of the considered structure, the temporal responses of the hot spots for all configurations were characterized by relatively strong pulse elongation (relative elongation was greater than or equal to 4.3%). At the same time, due to the reflection of the incident pulse and consequent interference, the temporal responses of most hot spots contained a few peaks for all configurations except for Config4. This shows that an in-depth preliminary optimization of the structure and different laser pulse shaping techniques is needed to obtain single-peak and unextended pulse responses. However, due to inaccuracies in the manufacturing of such structures (especially the size of nanoparticles and the distances between them), their use for ultrafast analysis presents certain difficulties. Nonetheless, the ultrashort temporal responses of all hot spots for Config4 were characterized by a single peak, albeit with a relatively large pulse elongation (absolute elongation of 4.94 fs and relative elongation of 234.1%).

These results suggest the need for further theoretical analysis and numerical optimization as well as the experimental verification of the structure with only six terminal nanoparticles (Config4). This will help us develop a deep understanding of the parametric behavior of the structure to improve its ultrashort characteristics. In addition, these efforts need to be complemented by the development of experimental means for realization of the proposed geometry. Up to now, focused ion beam etching has been mostly used for structuring of the apex of optical fiber tips coated with a thin metallic layer [48]. However, more recently a rich toolbox for the preparation of plasmonic nanostructures resembling the proposed geometry become available based on the self-assembly. So far it has been utilized in techniques including colloidal lithography [49] and DNA origami used for nanoscale control of docking of chemically synthesized metallic nanoparticles [50]. These techniques can be in principle used for direct structuring of the optical fiber-tip probes as well as on substrates followed by a transfer of the prepared structures to a fiber tip by template stripping [51].

## Acknowledgments

Yevhenii Morozov is grateful for the Zhejiang University of Technology (for Professor Zichun Le, in particular) for providing the Research Laboratory (according to the Contract dated 18 December 2017).

This work was supported in part by R&D Funding of the National Academy of Sciences of Ukraine under the grant agreement 0119U001105; in part by Special Funding of 'the Belt and Road' International Cooperation of Zhejiang Province under the grant agreement 2015C04005; and in part by Austrian Science Fund (FWF) under the grant agreement I 2647.

## ORCID iDs

Yevhenii M Morozov  <https://orcid.org/0000-0001-9689-8641>

## References

- [1] Bittle E G, Biacchi A J, Fredin L A, Herzing A A, Allison T C, Walker A R H and Gundlach D J 2019 Correlating anisotropic mobility and intermolecular phonons in organic semiconductors to investigate transient localization *Commun. Phys.* **2** 29
- [2] Daum R, Brauchle E M, Berrio D A C, Jurkowski T P and Schenke-Layland K 2019 Non-invasive detection of DNA methylation states in carcinoma and pluripotent stem cells using Raman microspectroscopy and imaging *Sci. Rep.* **9** 7014
- [3] Huang S, Pandey R, Barman I, Kong J and Dresselhaus M 2018 Raman enhancement of blood constituent proteins using graphene *ACS Photon.* **5** 2978–82
- [4] Usachov D Y et al 2017 Raman spectroscopy of lattice-matched graphene on strongly interacting metal surfaces *ACS Nano* **11** 6336–45
- [5] Sil S and Umapathy S 2014 Raman spectroscopy explores molecular structural signatures of hidden materials in depth: universal multiple angle Raman spectroscopy *Sci. Rep.* **4** 5308–14
- [6] Spezzazzini N et al 2014 Spectroscopic approach for dynamic bioanalyte tracking with minimal concentration information *Sci. Rep.* **4** 7013–9
- [7] Zhang J M et al 1998 Optical phonons in isotopic Ge studied by Raman scattering *Phys. Rev. B* **57** 1348–51
- [8] Cantarero A 2015 Raman scattering applied to materials science *Proc. Mater. Sci.* **9** 113–22
- [9] Wachsmann-Hogiu S, Weeks T and Huser T 2009 Chemical analysis *in vivo* and *in vitro* by Raman spectroscopy—from single cells to humans *Curr. Opin. Biotechnol.* **20** 63–73
- [10] Ember K J I et al 2017 Raman spectroscopy and regenerative medicine: a review *NPJ Regen. Med.* **2** 12
- [11] Yamamoto T et al 2018 Label-free evaluation of myocardial infarct in surgically excised ventricular myocardium by Raman spectroscopy *Sci. Rep.* **8** 14671
- [12] Gruenke N L et al 2016 Ultrafast and nonlinear surface-enhanced Raman spectroscopy *Chem. Soc. Rev.* **45** 2263–90
- [13] Yu B, Ge M, Li P, Xie Q and Yang L 2019 Development of surface-enhanced Raman spectroscopy application for determination of illicit drugs: towards a practical sensor *Talanta* **191** 1–10
- [14] Guo L et al 2019 Surface-enhanced Raman scattering (SERS) as a probe for detection of charge-transfer between TiO<sub>2</sub> and CdS nanoparticles *New J. Chem.* **43** 230–7
- [15] Chen C, Liu W, Tian S and Hong T 2019 Novel surface-enhanced Raman Spectroscopy techniques for DNA, protein and drug detection *Sensors* **19** 1712
- [16] Kumar N, Weckhuysen B M, Wain A J and Pollard A J 2019 Nanoscale chemical imaging using tip-enhanced Raman spectroscopy *Nat. Protoc.* **14** 1169–93
- [17] Lee J, Crampton K T, Tallarida N and Apkarian V A 2019 Visualizing vibrational normal modes of a single molecule with atomically confined light *Nature* **568** 78–82
- [18] Kukura P, Mccamant D W and Mathies R A 2017 Femtosecond stimulated Raman spectroscopy *Annu. Rev. Phys. Chem.* **58** 461–88
- [19] Ashner M N and Tisdale W A 2018 High repetition-rate femtosecond stimulated Raman spectroscopy with fast acquisition *Opt. Exp.* **26** 18331–40
- [20] Dietze D R and Mathies R A 2016 Femtosecond stimulated Raman spectroscopy *Chem. Phys. Chem.* **17** 1224–51
- [21] Kuramochi H, Takeuchi S and Tahara T 2016 Femtosecond time-resolved impulsive stimulated Raman spectroscopy using sub-7-fs pulses: apparatus and applications *Rev. Sci. Instrum.* **87** 043107
- [22] Abramczyk H, Brozek-Pluska B and Kopec M 2018 Polarized Raman microscopy imaging: capabilities and challenges for cancer research *J. Mol. Liq.* **259** 102–11
- [23] Sahoo S, Palai R and Katiyar R S 2011 Polarized Raman scattering in monolayer, bilayer, and suspended bilayer graphene *J. Appl. Phys.* **110** 044320
- [24] Chen K, Wu T, Wei H, Wu X and Li Y 2015 High spectral specificity of local chemical components characterization with multichannel shift-excitation Raman spectroscopy *Sci. Rep.* **5** 13952
- [25] Cordero E et al 2017 Evaluation of shifted excitation Raman difference spectroscopy and comparison to computational background correction methods applied to biochemical Raman spectra *Sensors* **17** 1724
- [26] Hanif S et al 2017 Nanopipette-based SERS aptasensor for subcellular localization of cancer biomarker in single cells *Anal. Chem.* **89** 9911–7
- [27] Vitol E A et al 2009 *In situ* intracellular spectroscopy with surface enhanced Raman spectroscopy (SERS)-enabled nanopipettes *ACS Nano* **3** 3529–36
- [28] Geßner R et al 2004 The application of a SERS fiber probe for the investigation of sensitive biological samples *Analyst* **129** 1193–9
- [29] Cao J, Zhao D and Mao Q 2017 A highly reproducible and sensitive fiber SERS probe fabricated by direct synthesis of closely packed AgNPs on the silanized fiber taper *Analyst* **142** 596–602
- [30] Wang J et al 2019 SERS-active fiber tip for intracellular and extracellular pH sensing in living single cells *Sens. Actuators B* **290** 527–34
- [31] Liu M et al 2019 Plasmonic tip internally excited via an azimuthal vector beam for surface enhanced Raman spectroscopy *Photon. Res.* **7** 526–31
- [32] Hutter T, Elliott S R and Mahajan S 2018 Optical fibre-tip probes for SERS: numerical study for design considerations *Opt. Exp.* **26** 15539
- [33] Taflove A and Hagness S C 2010 *Computational Electrodynamics: The Finite-Difference Time-Domain Method* (Boston, MA: Artech House Publishers)
- [34] Li Y 2017 *Plasmonics Optics: Theory and Applications* (Bellingham, WA: SPIE)
- [35] Palik E D 1985 *Handbook of Optical Constants of Solids* (New York: Academic)
- [36] Johnson P and Christy R W 1972 Optical constants of the noble metals *Phys. Rev. B* **6** 4370–9
- [37] Barchiesi D and Grosjes T 2014 Fitting the optical constants of gold, silver, chromium, titanium, and aluminum in the visible bandwidth *J. Nanophoton.* **8** 083097
- [38] Fisher D, Fraenkel M, Henis Z, Moshe E and Eliezer S 2001 Interband and intraband (Drude) contributions to femtosecond laser absorption in aluminum *Phys. Rev. E* **65** 016409
- [39] (Vancouver, Canada: FDTD Solutions, Lumerical Solutions, Inc.)

- [40] Zuloaga J, Prodan E and Nordlander P 2009 Quantum description of the plasmon resonances of a nanoparticle dimer *Nano Lett.* **9** 887–91
- [41] Tausenev A V et al 2005 Efficient source of femtosecond pulses and its use for broadband supercontinuum generation *Quantum Electron.* **35** 581–5
- [42] Piatkowski L, Accanto N and van Hulst N F 2016 Ultrafast meets ultrasmall: controlling nanoantennas and molecules *ACS Photon.* **3** 1401–14
- [43] Brinks D, Castro-Lopez M, Hildner R and van Hulst N F 2013 Plasmonic antennas as design elements for coherent ultrafast nanophotonics *Proc. Natl Acad. Sci. USA* **110** 18386–90
- [44] Morozov Y M, Lapchuk A S, Gorbov I V, Yao S and Le Z 2019 Optical plasmon nanostrip probe as an effective ultrashort pulse delivery system *Opt. Exp.* **27** 13031–52
- [45] Willingham B and Link S 2011 Energy transport in metal nanoparticle chains via sub-radiant plasmon modes *Opt. Exp.* **19** 6450–61
- [46] Krenn J R et al 1999 Squeezing the optical near-field zone by plasmon coupling of metallic nanoparticles *Phys. Rev. Lett.* **82** 2590–3
- [47] Huang J S, Voronine D V, Tuchscherer P, Brixner T and Hecht B 2009 Deterministic spatiotemporal control of optical fields in nanoantennas and plasmonic circuits *Phys. Rev. B* **79** 195441
- [48] Tuniz A and Schmidt M A 2018 Interfacing optical fibers with plasmonic nanoconcentrators *Nanophotonics* **7** 1279–98
- [49] Vogel N, Weiss C K and Landfester K 2012 From soft to hard: the generation of functional and complex colloidal monolayers for nanolithography *Soft Matter* **8** 84044–61
- [50] Julin S, Nummelin S, Kostiaainen M A and Linko V 2018 DNA nanostructure-directed assembly of metal nanoparticle superlattices *J. Nanopart. Res.* **20** 119
- [51] Ehtaiba J M and Gordon R 2018 Template-stripped nanoaperture tweezer integrated with optical fiber *Opt. Exp.* **26** 9607–13